PET Imaging of Tissue Factor in Pancreatic Cancer Using ^{64}Cu-Labeled Active Site–Inhibited Factor VII

Carsten H. Nielsen[1,2], Troels E. Jeppesen[2], Lotte K. Kristensen[1,2], Mette M. Jensen[1,2], Henrik H. El Ali[2], Jacob Madsen[2], Bo Wiinberg[3], Lars C. Petersen[3], and Andreas Kjaer[2]

[1]Minerva Imaging, Copenhagen, Denmark; [2]Department of Clinical Physiology, Nuclear Medicine & PET and Cluster for Molecular Imaging, Rigshospitalet and University of Copenhagen, Copenhagen, Denmark; and [3]Haemostasis Biology, Novo Nordisk A/S, Maalev, Denmark

Tissue factor (TF) is the main initiator of the extrinsic coagulation cascade. However, TF also plays an important role in cancer. TF expression has been reported in 53%–89% of all pancreatic adenocarcinomas, and the expression level of TF has in clinical studies correlated with advanced stage, increased microvessel density, metastasis, and poor overall survival. Imaging of TF expression is of clinical relevance as a prognostic biomarker and as a companion diagnostic for TF-directed therapies currently under clinical development. Factor VII (FVII) is the natural ligand to TF. The purpose of this study was to investigate the possibility of using active site–inhibited FVII (FVIIai) labeled with ^{64}Cu for PET imaging of TF expression. **Methods:** FVIIai was conjugated to 2-S-(4-isothiocyanatobenzyl)-1,4,7-triazacyclononane-1,4,7-triacetic acid (p-SCN-Bn-NOTA) and labeled with ^{64}Cu (^{64}Cu-NOTA-FVIIai). Longitudinal in vivo PET imaging was performed at 1, 4, 15, and 36 h after injection of ^{64}Cu-NOTA-FVIIai in mice with pancreatic adenocarcinomas (BxPC-3). The specificity of TF imaging with ^{64}Cu-NOTA-FVIIai was investigated in subcutaneous pancreatic tumor models with different levels of TF expression and in a competition experiment. In addition, imaging of orthotopic pancreatic tumors was performed using ^{64}Cu-NOTA-FVIIai and PET/MRI. In vivo imaging data were supported by ex vivo biodistribution, flow cytometry, and immunohistochemistry. **Results:** Longitudinal PET imaging with ^{64}Cu-NOTA-FVIIai showed a tumor uptake of 2.3 ± 0.2, 3.7 ± 0.3, 3.4 ± 0.3, and 2.4 ± 0.3 percentage injected dose per gram at 1, 4, 15, and 36 h after injection, respectively. An increase in tumor–to–normal-tissue contrast was observed over the imaging time course. Competition with unlabeled FVIIai significantly ($P < 0.001$) reduced the tumor uptake. The tumor uptake observed in models with different TF expression levels was significantly different from each other ($P < 0.001$) and was in agreement with the TF level evaluated by TF immunohistochemistry staining. Orthotopic tumors were clearly visible on the PET/MR images, and the uptake of ^{64}Cu-NOTA-FVIIai was colocalized with viable tumor tissue. **Conclusion:** ^{64}Cu-NOTA-FVIIai is well suited for PET imaging of tumor TF expression, and imaging is capable of distinguishing the TF expression level of various pancreatic tumor models.

Tissue factor (TF) is a 47-kDa glycosylated transmembrane protein consisting of a large extracellular domain and a short cytoplasmic domain. TF acts as the initiator of the extrinsic coagulation cascade. The zymogen factor VII (FVII) is the natural ligand to TF and gets activated to FVIIa on binding to TF. The TF-FVIIa complex further activates factor IX and factor X, eventually leading to fibrin deposition, platelet aggregation, and formation of a thrombus (1).

In addition to its role in the coagulation cascade, TF is associated with cancer (1–3). TF expression has been found in all solid tumors, and its expression has been linked to mutation of the K-ras oncogene, loss of p53 and PTEN tumor suppressor genes, and tumor hypoxia (4–7). TF is involved in angiogenesis, invasiveness, tumor growth, and antiapoptotic signaling primarily through phosphorylation of its cytoplasmic domain and activation of the protease-activated receptor-2 axis by the TF-FVIIa complex (1,3).

Pancreatic cancer accounts for about 3% of all newly diagnosed cancers, but because of its high mortality, pancreatic cancer accounts for 6% of all cancer-associated deaths in the developed world (8). About 85%–90% of pancreatic cancers are adenocarcinomas, with a 5-y survival of less than 10% (9,10).

Activating mutations in K-ras is the most common oncogenic mutation in pancreatic adenocarcinoma and is found in more than 90% of the patients (10). TF expression in pancreatic adenocarcinoma has been reported in 53%–89% of the tumors, and the expression level has been associated with advanced stage, increased microvessel density, metastasis, and poor survival (11–13).

Exploiting TF as a target for drug delivery has proven effective in xenograft mouse models. The use of FVII as a targeting domain conjugated with either the Fc portion of IgG or the potent curcumin analog EF24 has shown efficacy in human xenograft mouse models of melanoma and breast cancer (14,15). More recently, targeting of TF with an antibody-drug conjugate, Humax-TF-ADC, was reported (16,17). Antitumor efficacy was demonstrated in a wide range of TF-expressing tumors including complete tumor regression in a patient-derived xenograft model of pancreatic adenocarcinoma. Humax-TF-ADC is currently being evaluated in a clinical phase I

trial (NCT02001623), and encouraging clinical data on tolerability and safety were recently presented (*18*).

The development of companion diagnostics to identify patients with TF-positive tumors and thus eligibility for anti-TF therapies becomes clinically relevant as TF-targeted therapies emerge in the clinic. Here, we report the development and preclinical evaluation of a ^{64}Cu-labeled PET tracer for noninvasive imaging of tumor TF status. Active site–inhibited FVII (FVIIai), with a molecular weight of 50 kDa, which binds to TF with an affinity of approximately 1 nM (*19,20*), was conjugated with the 2-*S*-(4-isothiocyanatobenzyl)-1,4,7-triazacyclononane-1,4,7-triacetic acid (*p*-SCN-Bn-NOTA) chelator. In vivo PET imaging using ^{64}Cu-NOTA-FVIIai was performed in a panel of pancreatic adenocarcinoma xenograft mouse models established subcutaneously and orthotopically to demonstrate the ability of noninvasive imaging of tumor TF status.

MATERIALS AND METHODS

All chemicals were obtained from Sigma Aldrich unless stated otherwise. FVIIai was obtained from Novo Nordisk A/S. *p*-SCN-Bn-NOTA was purchased from Macrocyclics. ^{64}Cu was produced by The Hevesy Laboratory at DTU Nutech using the ^{64}Ni(p,n)^{64}Cu reaction and obtained in a dried formulation.

Synthesis of NOTA-FVIIai

A 10 mM stock solution of NOTA-Bn-NCS in *N*-(2-hydroxyethyl)piperazine-*N'*-(2-ethanesulfonic acid) (HEPES) buffer (50 mM HEPES, 10 mM $CaCl_2$, 150 mM NaCl, pH 8.7) was mixed, and the pH was adjusted to 8.7. *p*-SCN-Bn-NOTA stock solution (258 nmol, 25 mL) was added to FVIIai (1 mL, 51.2 nmol, adjusted to pH 8.7) and incubated for 20 h at 37°C. The reaction mixture was purified on a PD-10 desalting column (GE Healthcare) in 0.5-mL fractions in ammonium acetate buffer (0.1 M ammonium acetate, 10 mM $CaCl_2$, 150 mM NaCl, pH 5.5). The product was analyzed by high-performance liquid chromatography (HPLC) (supplemental materials and methods [available at http://jnm.snmjournals.org]). Two fractions containing the highest amount of NOTA-FVIIai were mixed, and the concentration was determined from a standard curve. The resulting NOTA-FVIIai was aliquoted in 150-μg portions and frozen at −80°C for later use. The amount of functional chelator bound to each protein was determined by cold copper titration as previously described (*21*). The experiment was performed in triplicate and analyzed by Image J software (National Institutes of Health).

Radiolabeling of NOTA-FVIIai

^{64}Cu was mixed with ultrapure water and left at room temperature for 30 min before use. Fifty to 80 μL (339–579 MBq) were added to a thawed vial of NOTA-FVIIai and incubated for 15 min at 25°C. The resulting ^{64}Cu-NOTA-FVIIai was purified by PD-10 in 0.5-mL fractions in gly-gly buffer (10 mM gly-gly, 150 mM NaCl, and 10 mM $CaCl_2$, pH 7.5). Two fractions, containing most of the radioactivity, were mixed and analyzed. The concentration and radiochemical purity of ^{64}Cu-NOTA-FVIIai were analyzed by HPLC and protein precipitation. The binding capability of ^{64}Cu-NOTA-FVIIai was evaluated in pull-down experiments with TF and FVII antibody-labeled Sepharose matrix. The stability of ^{64}Cu-NOTA-FVIIai was assessed in gly-gly buffer for up to 15 h (supplemental materials and methods). Furthermore, the stability was assessed in mouse serum as previously described (*22*); in brief, ^{64}Cu-NOTA-FVIIai (20 μL) was mixed with mouse serum (20 μL) and incubated for 0, 4, 15, and 36 h in triplicate. The samples were diluted 100 times with gly-gly buffer and analyzed with polyacrylamide gel electrophoresis under native conditions (7% Tris-acetate gel, Tris-acetate running buffer, 150V, 1 h). The gels were analyzed using Optiquant software (PerkinElmer) and stained with coomasie.

Cell Culture

PANC-1 (CRL-1469, LGC Standards; American Type Culture Collection [ATCC]), AsPC-1 (CRL-1682, LGC Standards; ATCC), BxPC-3 (CRL-1687, LGC Standards; ATCC), and BxPC-3-luc2 (PerkinElmer) were cultured in RPMI-1640 (AsPC-1 and BxPC-3) or Dulbecco modified Eagle medium (PANC-1) supplemented with 10% fetal bovine serum and 1% penicillin–streptomycin (Invitrogen) at 37°C and 5% CO_2. Cells tested negative for *Mycoplasma* and a panel of murine pathogens. Cell surface expression of TF was measured by flow cytometry as previously described (*19*).

Cell Binding

PANC-1 and BxPC-3 cells were seeded at 200,000 cells/well in a 24-well plate and cultured overnight. The culture medium was aspirated, and 300 μL of approximately 1.5 nM of ^{64}Cu-NOTA-FVIIai in binding buffer (phosphate-buffered saline with Ca^{2+} and Mg^{2+} and 1% bovine serum albumin) were added per well. Competition was performed with 1,000-fold-excess FVIIai. The cells were incubated for 2 h at 4°C, washed twice (binding buffer), lysed (50 mM Tris-HCl, 150 mM NaCl, 1% Triton-X, 1 mM ethylenediaminetetraacetic acid, 1% protease inhibitor, 0.4 mM phenylmethanesulfonyl fluoride), and counted for radioactivity in a γ-counter (Wizard^2; PerkinElmer). The amount of radioactivity in each sample was normalized to total protein determined with the BCA assay using the manufacturer's protocol (BCA Protein Assay Kit; Thermo Scientific). Each condition was performed in triplicate.

Animal Models

Cells in their exponential growth phase and at 80%–90% confluence were harvested by trypsinization and resuspended in 1:1 medium and Matrigel (BD Biosciences) at 5×10^7 cells/mL. Subcutaneous tumors were established in female NMRI nude mice (Taconic) by inoculation of 5×10^6 cells in 100 μL on each flank above the hind limbs in the subcutaneous space.

Orthotopic tumor models were established as previously described (*23*). In brief, NMRI mice were anesthetized with sevoflurane, and an incision was made in the left flank region distal of the pancreas. The spleen and pancreas were partly externalized, and 5×10^5 cells in 1:1 medium and Matrigel in a total volume of 25 mL were slowly injected in the midbody of the pancreas. The spleen and pancreas were gently internalized and the abdominal layer closed with absorbable sutures. Finally, the skin was sutured with absorbable sutures. Postoperative care consisted of buprenorphine (0.1 mg/kg) subcutaneously 3 times per day for 1 d and carprofen (5 mg/kg) subcutaneously 1 time per day for 3 d. All animal experiments were performed under a protocol approved by the National Animal Experiments Inspectorate.

Small-Animal Imaging

Longitudinal small-animal PET/CT imaging (Inveon Multimodality PET/CT scanner; Siemens) was performed with BxPC-3 tumor–bearing mice (*n* = 4) injected intravenously with 5.6–11.2 MBq of ^{64}Cu-NOTA-FVIIai in 150 μL. Competition with unlabeled FVIIai was performed in a group of mice (*n* = 3) that received 500 μg of FVIIai before ^{64}Cu-NOTA-FVIIai. Mice were anesthetized with sevoflurane (Abbott Laboratories) during injection and PET/CT imaging. PET data were acquired in list mode at 1, 4, 15, and 36 h (acquisition time, 300, 600, 900, and 1,200 s, respectively) after injection, and images were reconstructed using a 3-dimensional maximum a posteriori algorithm with CT-based attenuation correction. CT images were acquired using 180 projections, 65 kV, 500 μA, and 400 ms exposure and reconstructed with an isotropic voxel size of 104 μm. Images were analyzed using the Inveon software (Siemens). Region of interests (ROIs) were drawn manually over the tumor regions and other organs based on the CT images, and the uptake of ^{64}Cu-NOTA-FVIIai was quantified as percentage injected dose per gram of tissue (%ID/g). Mice were euthanized after the imaging

session and the tumors resected, cut in half, and either snap-frozen in liquid nitrogen or fixed in 4% paraformaldehyde for 24 h and transferred to 70% ethanol for molecular analysis.

Anatomic MR images of mice ($n = 3$) with orthotopic tumors were acquired on a BioSpec 7T/30 cm system (Bruker) equipped with a mouse body volume transmit receive coil. Images were acquired with the ParaVision 6 software with the following settings: TurboRARE-T$_2$, repetition time, 899.2 ms; echo time, 27 ms; 4 averages; slice thickness, 0.75 mm; interslice distance, 0.80 mm; and in-plane pixel size, 156 × 156 μm. Images were acquired in the axial and sagittal planes with respiratory gating enabled. The mouse was transferred to the PET/CT scanner on the MR bed for subsequent imaging. Fusion of the PET/CT and MR images was performed using the Inveon Software.

Biodistribution

Conventional ex vivo biodistribution was performed in a subgroup of animals after each of the imaging time points ($n = 4$/time point). Mice were euthanized, the tumors and organs were resected and weighted, and the radioactivity was counted in a γ-counter.

Radiation Dosimetry Estimation

Data from the ex vivo biodistribution performed at 1, 4, 15, and 36 h after injection of ^{64}Cu-NOTA-FVIIai were used to estimate the human dosimetry. Estimations were made for a male and female phantom using the OLINDA/EXM version 1 software (24). A dynamic bladder model was applied with a biologic half-life of 1.5 h, an elimination fraction of 75%, and a void interval of 5 h.

Immunohistochemistry

Staining was performed as previously described (19); in brief: formalin-fixed paraffin-embedded tumors were sectioned at 4 μm, deparaffinized, rehydrated, and microwaved in citrate buffer, pH 6, for epitope retrieval. Sections were blocked with 2% bovine serum albumin in phosphate-buffered saline, and primary antibody against human tissue factor CD142 (4508, American Diagnostica Inc.) was added at 1:800 dilution for 1 h at room temperature. Primary antibody was detected by the EnVision+ System-HRP Labeled Polymer and Liquid DAB+ Substrate Chromogen System (Dako) before counterstaining with Mayer's Hematoxylin (Region H Apotek).

Statistical Analysis

Unless stated otherwise, data are expressed as mean ± SEM. The effect of competition on the biodistribution data was evaluated by Multiple t tests with correction for multiple comparisons (Holm-Sidak). A 1-way ANOVA with post hoc test corrected for multiple comparisons (Tukey) was applied to test the biodistribution organ ratios and the uptake values in the different pancreatic cancer models. P values of 0.05 or less were considered statistically significant. Statistical analyses were performed using GraphPad Prism 6.0 d (GraphPad Software).

RESULTS

Radiochemistry

Functional chelator to protein amount was measured to 3.0 ± 0.18 ($n = 3$). ^{64}Cu-NOTA-FVIIai was produced in 78.5% ± 2.4% decay-corrected radiochemical yield, with a radiochemical purity of greater than 99% and 97.3% ± 0.6% determined by analytic HPLC and protein precipitation, respectively (Fig. 1). The specific radioactivity was 176.6 ± 17.8 GBq/μmol, and the protein concentration was 99.9 ± 8.5 μg/mL. Pull-down experiments showed that binding of ^{64}Cu-NOTA-FVIIai to TF and to the F1A2 FVII antibody (72.4% ± 1.7% and 87.0% ± 0.2%, respectively) was comparable to the binding of unlabeled FVIIai

(87% ± 5% and 91% ± 2%, respectively). All the above data are average ± SEM, $n = 3$. The stability of ^{64}Cu-FVIIai-NOTA in gly-gly buffer was greater than 95% over 15 h, and the stability in mouse serum was 82%, 72%, and 44% after 4, 15, and 36 h of incubation, respectively.

The binding of ^{64}Cu-NOTA-FVIIai to TF was investigated in a cell-binding assay with the TF-positive BxPC-3 and TF-negative PANC-1 cell lines (Fig. 1C). The binding of ^{64}Cu-NOTA-FVIIai to BxPC-3 cells was significantly higher than to PANC-1 cells (3,126 ± 230 vs. 150 ± 26 cpm/μg protein, $P \leq 0.001$). Competition with unlabeled FVIIai significantly blocked the binding to BxPC-3 cells compared with no competition (13 ± 0.4 vs. 3,126 ± 230 cpm/μg protein, $P \leq 0.001$).

Longitudinal Small-Animal PET/CT

The temporal in vivo distribution of ^{64}Cu-NOTA-FVIIai was assessed by longitudinal PET/CT imaging of mice with subcutaneous
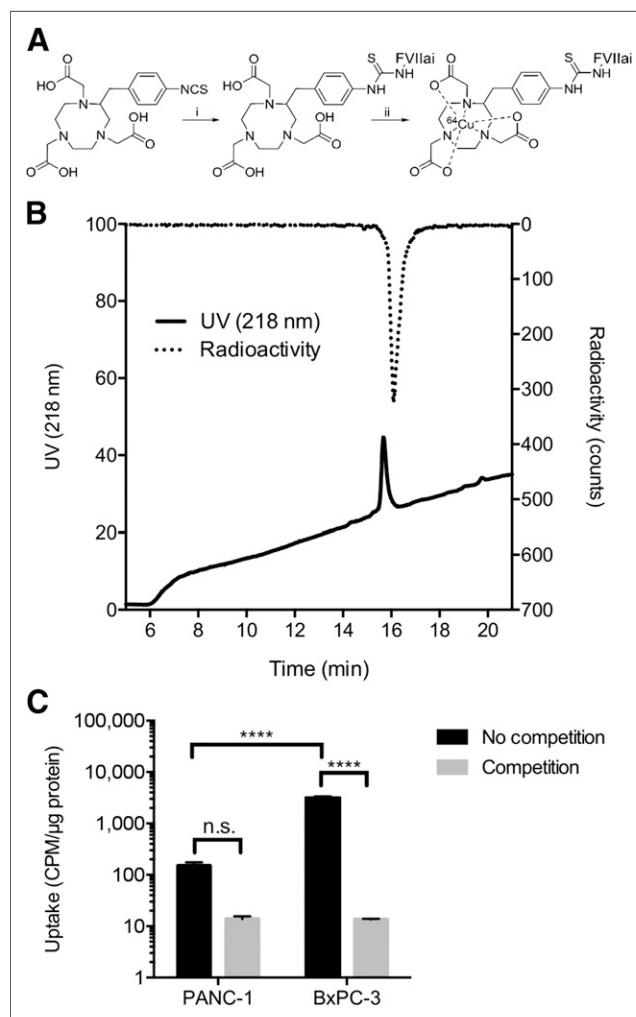

FIGURE 1. (A) Labeling of ^{64}Cu-NOTA-FVIIai. (i) HEPES, pH 8.7, FVIIai, 37°C, 20 h. (ii) ^{64}CuCl$_2$, NH$_4$OAc, pH 5.5, 15 min at room temperature. (B) High-performance liquid chromatogram of ^{64}Cu-NOTA-FVIIai after PD-10 purification in gly-gly buffer. (C) In vitro cell binding of ^{64}Cu-NOTA-FVIIai to PANC-1 and BxPC-3 cells with and without competition with unlabeled FVIIai. Uptake is expressed as counts per minute (cpm) normalized to total protein in μg. n.s. = not significant. ****$P < 0.0001$.

pancreatic adenocarcinoma BxPC-3 tumors. Coronal and axial images of the same mouse imaged at 1, 4, 15, and 36 h after injection of ^{64}Cu-NOTA-FVIIai are shown in Figure 2A and the corresponding maximum-intensity-projection image at 36 h in Figure 2B. Quantitative data on the temporal uptake are depicted in Figures 2C and 2D.

High accumulation of ^{64}Cu-NOTA-FVIIai was seen in the liver, kidney, and blood along with some tumor uptake at the 1-h imaging time point. ^{64}Cu-NOTA-FVIIai was excreted through both the kidneys and the hepatobiliary system (Fig. 2A), and the blood retention half-life was 1.6 h when modeled as a 1-phase decay. A significant increase in tumor–to–normal-tissue contrast was observed throughout the imaging time course (Figs. 2C and 2D), and the tumors were clearly visible at 36 h (Fig. 2B). However, no further improvement in tumor-to-muscle ratio was observed from 15 to 36 h. Besides uptake in the liver, kidney, and tumors, focal uptake was observed in the major joints.

The intratumor uptake was rather heterogeneous. The average tumor uptake quantified by ROI analysis was 2.3 ± 0.2, 3.7 ± 0.3, 3.4 ± 0.3, and 2.4 ± 0.3 %ID/g at 1, 4, 15, and 36 h after injection, respectively (Fig. 2E). In comparison, the maximum uptake within the tumors was significantly higher (6.6 ± 1.1, 9.5 ± 1.9, 9.4 ± 1.9, and 7.4 ± 1.4 %ID/g at 1, 4, 15, and 36 h, respectively).

Biodistribution and Competition

Conventional ex vivo biodistribution was performed at each of the imaging time points (Fig. 3A). The biodistribution results confirmed the data obtained by in vivo PET imaging and showed a relatively fast blood clearance and high retention in the liver, kidney, and tumor. An increase in tumor-to-blood, tumor-to-muscle, and tumor-to-pancreas ratios was observed throughout the time course of the biodistribution (Fig. 3B). The ratios observed at 36 h compared with 15 h were all significantly higher ($P \leq 0.05$). A competition experiment with unlabeled FVIIai was performed in a separate group of mice. Injection of unlabeled FVIIai before ^{64}Cu-NOTA-FVIIai injection significantly reduced the tumor uptake ($P \leq 0.001$), whereas the uptake in the other organs was unchanged, indicating a specific uptake of ^{64}Cu-NOTA-FVIIai in the tumors (Fig. 3C).

On the basis of the longitudinal PET and biodistribution data, it was decided to further evaluate ^{64}Cu-NOTA-FVIIai for PET imaging 15 h after injection in a panel of pancreatic adenocarcinoma mouse models.

Specific Imaging of TF in Panel of Subcutaneous Pancreatic Tumors

The ability of ^{64}Cu-NOTA-FVIIai to image TF expression was tested in 3 pancreatic adenocarcinoma models established by subcutaneous injection of PANC-1, AsPC-1, or BxPC-3 cells that had low, intermediate, and high TF expression, respectively. PET/CT images acquired 15 h after injection of ^{64}Cu-NOTA-FVIIai showed low, medium, and high uptake of ^{64}Cu-NOTA-FVIIai in the tumors (Fig. 4A), which was confirmed by quantitative ROI analysis of the mean and maximum tumor uptake (Figs. 4C and 4D). The mean tumor uptake was 1.0 ± 0.05, 1.7 ± 0.05, and 3.2 ± 0.2 %ID/g for PANC-1, AsPC-1, and BxPC-3 models, respectively. A similar pattern was observed for the maximum uptake within the tumors, which was 2.2 ± 0.1, 4.1 ± 0.1, and 7.5 ± 0.5 %ID/g for the PANC-1, AsPC-1, and BxPC-3 models, respectively. Any of the 3 models showed mean and maximum tumor uptake values that were each significantly different ($P \leq 0.001$) from uptake values of the 2 other tumor models. The in vivo uptake pattern was confirmed by flow cytometry of the cell lines before tumor inoculation (Supplemental Fig. 1) and by immunohistochemistry staining for TF in tumor sections (Fig. 4D).

Imaging of Orthotopic Pancreatic Tumors

[64]Cu-NOTA-FVIIai PET/MR was performed with an orthotopic pancreatic adenocarcinoma model to test if it was possible to visualize the tumors when located at their natural position near high-background organs such as the liver and kidneys. T2-weighted MR imaging was applied to visualize the orthotopic BxPC-3-luc2 tumors. The tumors appeared as a round mass with a central area with high signal intensity corresponding to a fluid-filled area likely due to necrosis (Fig. 5). ^{64}Cu-NOTA-FVIIai PET was able to clearly visualize the orthotopic tumors despite the high background in the kidneys. The tumor uptake was heterogeneous and with a spheric shape, which aligned with the area of viable tumor tissue on the fused PET/MR images.
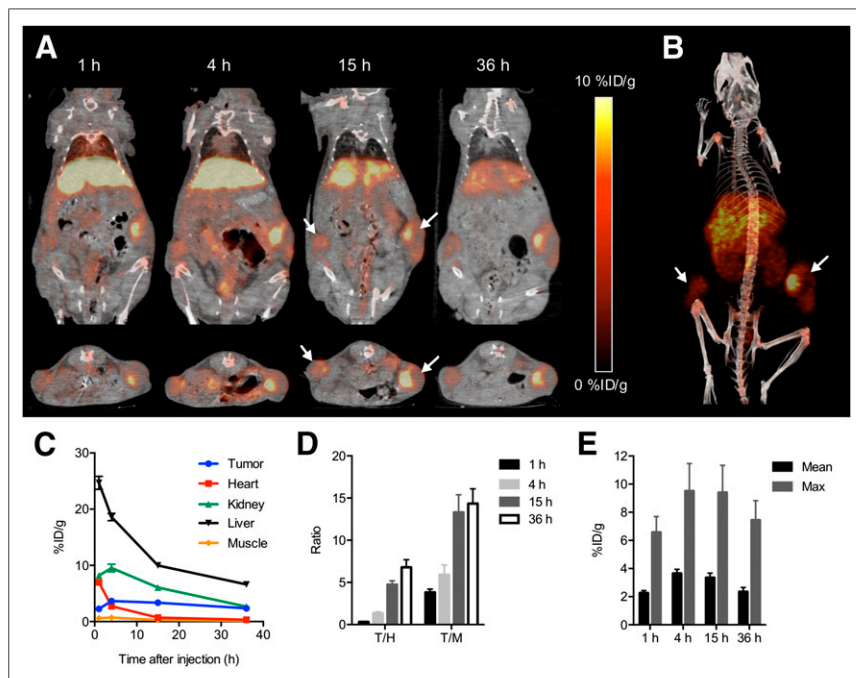

FIGURE 2. Longitudinal ^{64}Cu-NOTA-FVIIai PET imaging of mice with subcutaneous BxPC-3 tumors ($n = 4$ at 1, 4, and 15 h and $n = 3$ at 36 h). (A) Representative coronal and axial PET/CT images of same mouse imaged at 1, 4, 15, and 36 h after injection of ^{64}Cu-NOTA-FVIIai are shown. Arrows designate tumors. (B) Maximum-intensity-projection image at 36 h. (C) Image-derived biodistribution of ^{64}Cu-NOTA-FVIIai in major organs. (D) Tumor-to-heart (T/H) and tumor-to-muscle (T/M) ratios at 1, 4, 15, and 36 h. (E) Mean and maximum (max) uptake within tumors.
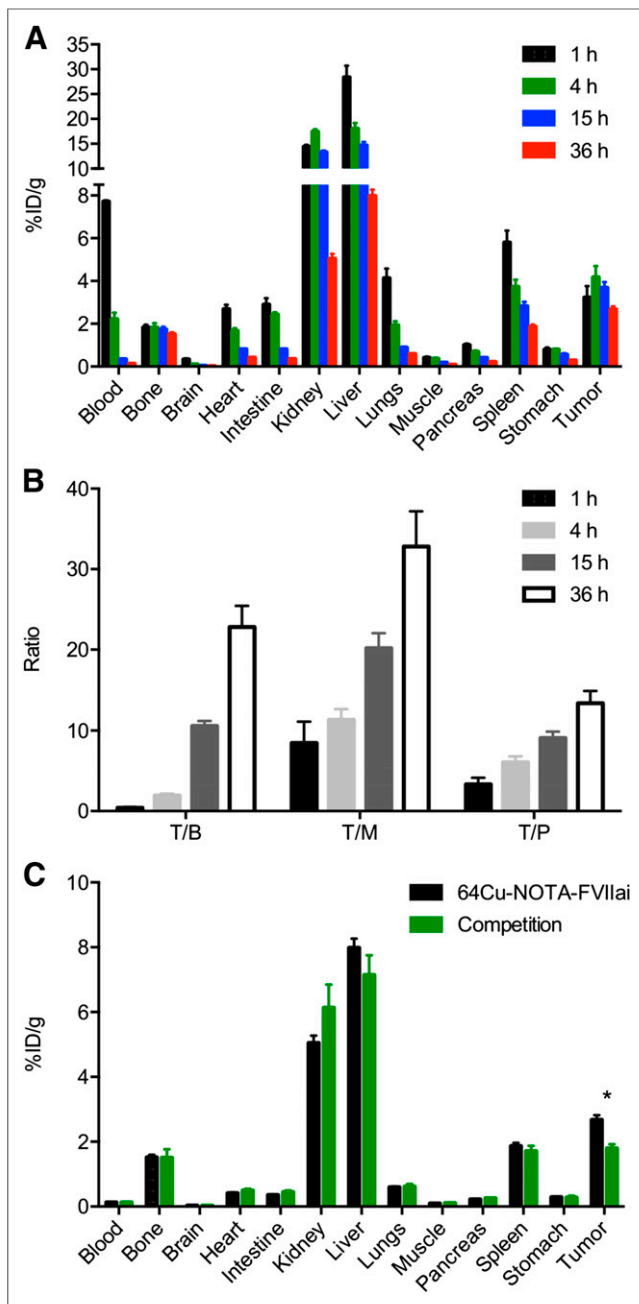
0.0678 and 0.0546 mSv/MBq for females and 0.0521 and 0.0412 mSv/MBq for males.

DISCUSSION

TF-directed therapies have shown promising results in preclinical testing, and encouraging clinical data have recently been presented (*18*). Thus, from a patient management perspective it becomes important to identify patients eligible for TF-targeted therapies. Here we report the development and evaluation of ^{64}Cu-NOTA-FVIIai for noninvasive PET imaging of tumor TF status in pancreatic cancer. PET imaging holds great promise in the area of companion diagnostics because it allows whole-body assessment of, for example, TF expression. Hence assessment of TF expression of the primary tumor and metastases can be performed in the same examination.

We have previously demonstrated proof of concept for PET imaging of TF expression with ^{18}F-labeled FVIIai (*19*). The results showed improved image contrast at the late time points, with the highest tumor uptake and image contrast obtained 4 h after injection of ^{18}F-FVIIai. An obvious next step was to investigate whether FVIIai labeled with an isotope with a longer half-life, which enables delayed imaging, would improve the tumor uptake and image contrast. In the current study, we therefore explored the potential of delayed imaging of tumor TF expression using ^{64}Cu-NOTA-FVIIai PET. To our knowledge, this is the first report on using FVIIai labeled with ^{64}Cu, and ^{64}Cu-NOTA-FVIIai was

FIGURE 3. (A) Ex vivo biodistribution at 1, 4, 15, and 36 h after injection of ^{64}Cu-NOTA-FVIIai in mice with subcutaneous BxPC-3 tumors (*n* = 4). (B) Tumor-to-blood (T/B), tumor-to-muscle (T/M), and tumor-to-pancreas (T/P) ratios at 1, 4, 15, and 36 h. (C) Biodistribution at 36 h with and without competition with unlabeled FVIIai (*n* = 4). *P* < 0.05.

Dosimetry

The predicted human dose was estimated with the OLINDA software based on the ex vivo biodistribution performed at 1, 4, 15, and 36 h after injection of ^{64}Cu-NOTA-FVIIai. The predicted human dosimetry for ^{64}Cu-NOTA-FVIIai is shown in Table 1. The organs predicted to receive the highest radiation burden for both males and females were the urinary bladder wall (0.401 and 0.300 mSv/MBq), followed by the liver (0.140 and 0.111 mSv/MBq). The mean effective dose equivalent and effective dose were estimated to
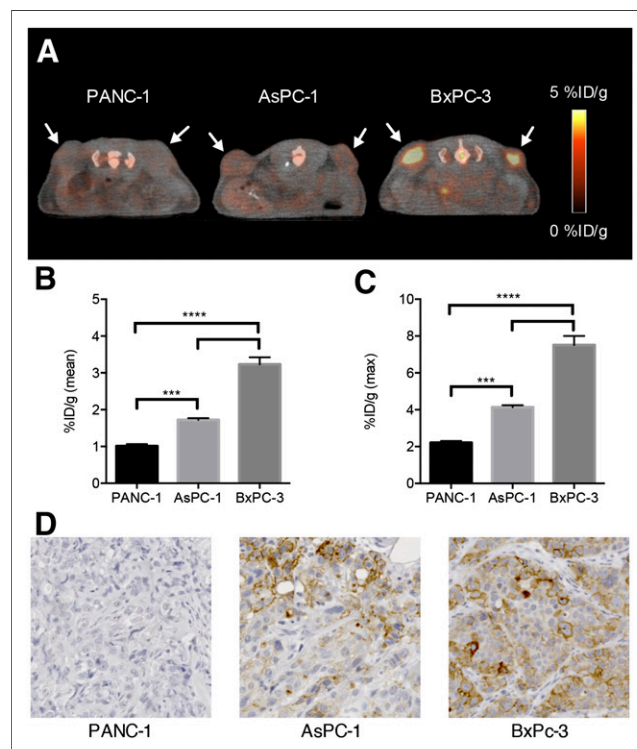

FIGURE 4. ^{64}Cu-NOTA-FVIIai PET/CT of mice with subcutaneous pancreatic tumors with different TF expression levels (*n* = 4). (A) Representative PET/CT images of mice with PANC-1, AsPC-1, and BxPC-3 tumors. Arrows designate tumors. Quantitative ROI analysis of mean (B) and maximum (C) tumor uptake (*n* = 8). (D) TF immunohistochemistry staining of representative tumor sections for each model. ***P* < 0.001. *****P* < 0.0001.
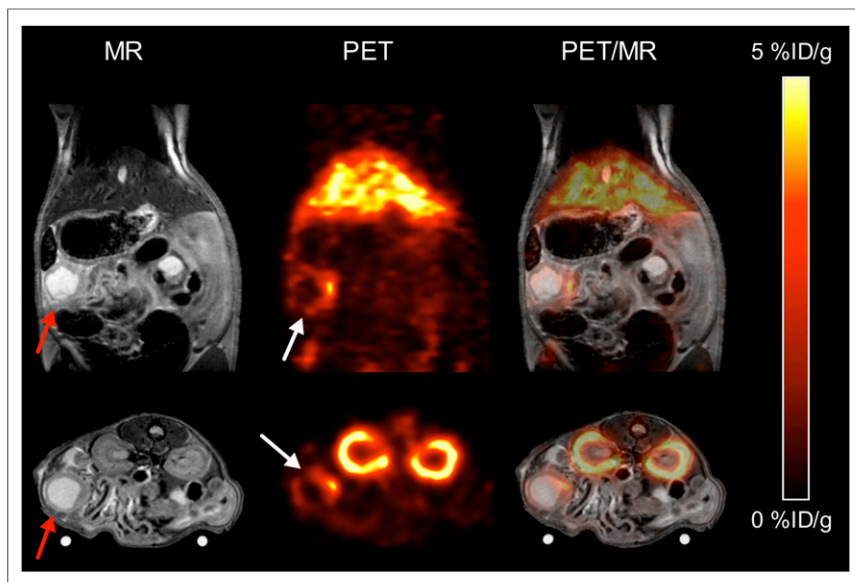
FIGURE 5. PET/MR imaging of TF expression in a mouse with an orthotopic BxPC-3-luc2 pancreatic tumor. Anatomic T2-weighted MR images show pancreatic tumor (red arrow). Tumor uptake of ^{64}Cu-NOTA-FVIIai was seen on PET images (white arrow), which colocalized with tumor on coregistered PET/MR images ($n = 3$).

able to clearly delineate TF-expressing tumors established both subcutaneously and orthotopically.

In the current study, we report a mean tumor uptake of 3.7 ± 0.3 %ID/g at 4 h after injection, which was significantly higher than the tumor uptake of ^{18}F-FVIIai at 4 h (2.5 ± 0.3 %ID/g, $P < 0.05$) (19). This higher tumor uptake could be attributed to the fact that the tumors in the current study were larger than those in the ^{18}F-FVIIai study (data not shown), increasing the possibility of hypoxic tumor areas and elevated hypoxia-induced TF expression (7). Because of the longer half-life of ^{64}Cu (12.7 h) than ^{18}F (109.7 min), we were also able to delay the image acquisition substantially beyond 4 h. We observed an increase in tumor-to-muscle contrast in the PET images when going from 4 to 15 h after injection of ^{64}Cu-NOTA-FVIIai. The increase in tumor-to-muscle ratio over time was confirmed by the biodistribution data, for which the highest contrast was seen at 36 h after injection. However, we did not see any clear increase in tumor-to-muscle ratio from 15 to 36 h on the PET images, and most the image acquisitions were thus performed at 15 h. Imaging of tumor TF expression in a panel of subcutaneous pancreatic tumors 15 h after injection of ^{64}Cu-NOTA-FVIIai showed that the uptake in the tumors was in agreement with TF expression in the tumors evaluated with immunohistochemistry staining. Also, injection of unlabeled FVIIai before ^{64}Cu-NOTA-FVIIai administration significantly reduced the uptake in the tumors. Together, these results support that specific imaging of tumor TF expression is possible by ^{64}Cu-NOTA-FVIIai PET.

The longer half-life of ^{64}Cu also enabled us to investigate the tumor retention of ^{64}Cu-NOTA-FVIIai over an extended time period, which provided insightful data on the potential of using FVIIai labeled with, for example, ^{177}Lu or ^{90}Y for targeted radionuclide therapy. ^{64}Cu-NOTA-FVIIai exhibited good tumor retention, with a tumor washout from 4 to 36 h after injection of 35% (3.7 ± 0.3 vs. 2.4 ± 0.3 %ID/g). In comparison, therapeutic efficacy was demonstrated in preclinical models with a ^{177}Lu-labeled peptide that showed a much faster tumor washout and hence comparatively lower radiation dose to the tumor (25,26). Delivery of a higher radiation dose to the tumors can be achieved using radiolabeled antibodies. However, the absorbed dose in the red bone marrow usually becomes a limitation because of the prolonged blood circulation of full-length antibodies (27). In contrast, the blood retention half-life of ^{64}Cu-NOTA-FVIIai was estimated to be 1.6 h based on the in vivo PET data. The short circulation and the prolonged tumor retention together merit further development of FVIIai for targeted radionuclide therapy.

PET imaging of TF has previously been investigated using a ^{64}Cu-labeled TF antibody and its Fab fragment (28,29). A superior tumor uptake of 16.5 ± 2.6 %ID/g 48 h after injection of the ^{64}Cu-labeled full-length antibody was reported (28). Despite the impressive tumor uptake, the tumor-to-muscle ratio was similar to what we report because of the long circulation of full-length antibodies. The tumor uptake reported for the antibody Fab fragment was slightly higher, whereas the tumor-to-muscle ratio was about 50% lower than our results (29).

High uptake was seen in the liver and kidneys throughout the imaging time course. This result is similar to other reports and was most likely due to clearance of intact ^{64}Cu-NOTA-FVIIai, instability of the chelation complex, and accumulation of radiometabolites (30,31). As noted in the publication by Hong et al. (28) on a ^{64}Cu-labeled TF antibody, imaging of orthotopic pancreatic tumors with ^{64}Cu-labeled ligands represents a challenge because of the proximity of the pancreas to high-background organs such as the liver and kidneys. However, in the current work we demonstrated that imaging of orthotopic pancreatic tumors was indeed possible. The uptake of ^{64}Cu-NOTA-FVIIai within the tumors on the coregistered PET/MR images was nicely colocalized with areas of viable tumor.

The cross reactivity between human FVIIai and murine TF is rather low (19,32,33), implying that the current study does not necessarily give a good estimate of the background uptake of ^{64}Cu-NOTA-FVIIai in normal tissues because of the absence of human TF outside the tumor regions. The issue is currently being addressed in an animal model that exhibits cross reactivity between TF and human FVIIai before clinical translation.

In the clinical setting, patients will receive less than 0.1 mg of ^{64}Cu-NOTA-FVIIai with an expected patient dose of 200 MBq and the reported specific radioactivity. This mass of FVIIai should be of no concern because FVIIai has previously been evaluated in clinical trials as an anticoagulant. A single dose up to 0.4 mg/kg, almost 300 times more than we plan to use for PET imaging, was reported to be safe (34). Human dosimetry estimates were obtained using the OLINDA software for males and females. With an injected dose of 200 MBq, a patient was estimated to receive an effective dose of 8.2 mSv (male) and 10.9 mSv (female), which is about twice that of ^{18}F-FDG (35) but not considered prohibitive for the further development of ^{64}Cu-NOTA-FVIIai as an imaging agent.

TABLE 1
Predicted Human Dosimetry for ^{64}Cu-NOTA-FVIIai (mSv/MBq)

Organ	Female	Male
Adrenals	3.72E–02	2.72E–02
Brain	5.91E–03	4.18E–03
Breasts	2.85E–02	2.07E–02
Gallbladder wall	4.00E–02	3.14E–02
Lower large intestine wall	3.79E–02	2.71E–02
Small intestine	4.30E–02	3.43E–02
Stomach wall	3.32E–02	2.44E–02
Upper large intestine wall	3.67E–02	2.69E–02
Heart wall	8.14E–02	6.41E–02
Kidneys	9.94E–02	7.82E–02
Liver	1.40E–01	1.11E–01
Lungs	2.30E–02	1.75E–02
Muscle	1.36E–02	1.04E–02
Ovaries	3.71E–02	
Pancreas	2.04E–02	1.62E–02
Red marrow	2.87E–02	2.26E–02
Osteogenic cells	4.52E–02	4.97E–02
Skin	2.58E–02	1.86E–02
Spleen	3.43E–02	2.76E–02
Testes		2.29E–02
Thymus	3.23E–02	2.29E–02
Thyroid	2.85E–02	2.09E–02
Urinary bladder wall	4.01E–01	3.00E–01
Uterus	4.14E–02	
Total body	3.57E–02	2.59E–02
Effective dose equivalent	6.78E–02	5.21E–02
Effective dose	5.46E–02	4.12E–02

CONCLUSION

Noninvasive specific imaging of tumor TF expression was achieved using ^{64}Cu-NOTA-FVIIai PET imaging. High uptake of ^{64}Cu-NOTA-FVIIai was seen in TF-positive tumors. Delayed imaging of ^{64}Cu-NOTA-FVIIai improved the tumor–to–normal-tissue contrast, and orthotopic tumors were clearly visible on PET/MR images acquired 15 h after injection. Together with the favorable dosimetry, the data fully support further development and clinical translation of ^{64}Cu-NOTA-FVIIai as a companion diagnostics for TF-directed therapies and potentially as a theranostics for targeted radionuclide therapy.

DISCLOSURE

ACKNOWLEDGMENT

REFERENCES

1. van den Berg YW, Osanto S, Reitsma PH, Versteeg HH. The relationship between tissue factor and cancer progression: insights from bench and bedside. *Blood.* 2012;119:924–932.
2. Kasthuri RS, Taubman MB, Mackman N. Role of tissue factor in cancer. *J Clin Oncol.* 2009;27:4834–4838.
3. Åberg M, Siegbahn A. Tissue factor non-coagulant signaling: molecular mechanisms and biological consequences with a focus on cell migration and apoptosis. *J Thromb Haemost.* 2013;11:817–825.
4. Yu JL, May L, Lhotak V, et al. Oncogenic events regulate tissue factor expression in colorectal cancer cells: implications for tumor progression and angiogenesis. *Blood.* 2005;105:1734–1741.
5. Rao B, Gao Y, Huang J, et al. Mutations of p53 and K-ras correlate TF expression in human colorectal carcinomas: TF downregulation as a marker of poor prognosis. *Int J Colorectal Dis.* 2011;26:593–601.
6. Regina S, Valentin J-B, Lachot S, Lemarié E, Rollin J, Gruel Y. Increased tissue factor expression is associated with reduced survival in non-small cell lung cancer and with mutations of TP53 and PTEN. *Clin Chem.* 2009;55:1834–1842.
7. Rong Y, Post DE, Pieper RO, Durden DL, Van Meir EG, Brat DJ. PTEN and hypoxia regulate tissue factor expression and plasma coagulation by glioblastoma. *Cancer Res.* 2005;65:1406–1413.
8. Torre LA, Bray F, Siegel RL, Ferlay J, Lortet-Tieulent J, Jemal A. Global cancer statistics, 2012. *CA Cancer J Clin.* 2015;65:87–108.
9. Cid-Arregui A, Juarez V. Perspectives in the treatment of pancreatic adenocarcinoma. *World J Gastroenterol.* 2015;21:9297–9316.
10. Ryan DP, Hong TS, Bardeesy N. Pancreatic adenocarcinoma. *N Engl J Med.* 2014;371:1039–1049.
11. Kakkar AK, Lemoine NR, Scully MF, Tebbutt S, Williamson RC. Tissue factor expression correlates with histological grade in human pancreatic cancer. *Br J Surg.* 1995;82:1101–1104.
12. Nitori N, Ino Y, Nakanishi Y, et al. Prognostic significance of tissue factor in pancreatic ductal adenocarcinoma. *Clin Cancer Res.* 2005;11:2531–2539.
13. Khorana AA, Ahrendt SA, Ryan CK, et al. Tissue factor expression, angiogenesis, and thrombosis in pancreatic cancer. *Clin Cancer Res.* 2007;13:2870–2875.
14. Hu Z, Sun Y, Garen A. Targeting tumor vasculature endothelial cells and tumor cells for immunotherapy of human melanoma in a mouse xenograft model. *Proc Natl Acad Sci USA.* 1999;96:8161–8166.
15. Shoji M, Sun A, Kisiel W, et al. Targeting tissue factor-expressing tumor angiogenesis and tumors with EF24 conjugated to factor VIIa. *J Drug Target.* 2008;16:185–197.
16. Breij ECW, de Goeij BECG, Verploegen S, et al. An antibody-drug conjugate that targets tissue factor exhibits potent therapeutic activity against a broad range of solid tumors. *Cancer Res.* 2014;74:1214–1226.
17. de Goeij BECG, Satijn D, Freitag CM, et al. High turnover of tissue factor enables efficient intracellular delivery of antibody-drug conjugates. *Mol Cancer Ther.* 2015;14:1130–1140.
18. Lassen UN, Hong DS, Diamantis N, et al. A phase I, first-in-human study to evaluate the tolerability, pharmacokinetics and preliminary efficacy of HuMax-tissue factor-ADC (TF-ADC) in patients with solid tumors. *ASCO Meeting Abstracts.* 2015;33:2570.
19. Nielsen CH, Erlandsson M, Jeppesen TE, et al. Quantitative PET imaging of tissue factor expression using ^{18}F-labeled active site-inhibited factor VII. *J Nucl Med.* 2016;57:89–95.
20. Sorensen BB, Persson E, Freskgård PO, et al. Incorporation of an active site inhibitor in factor VIIa alters the affinity for tissue factor. *J Biol Chem.* 1997;272:11863–11868.

21. Cai W, Chen K, Mohamedali KA, et al. PET of vascular endothelial growth factor receptor expression. *J Nucl Med.* 2006;47:2048–2056.

22. Erlandsson M, Nielsen CH, Jeppesen TE, et al. Synthesis and characterization of ^{18}F-labeled active site inhibited factor VII (ASIS). *J Labelled Comp Radiopharm.* 2015;58:196–201.

23. Kim MP, Evans DB, Wang H, Abbruzzese JL, Fleming JB, Gallick GE. Generation of orthotopic and heterotopic human pancreatic cancer xenografts in immunodeficient mice. *Nat Protoc.* 2009;4:1670–1680.

24. Stabin MG, Siegel JA. Physical models and dose factors for use in internal dose assessment. *Health Phys.* 2003;85:294–310.

25. Persson M, Rasmussen P, Madsen J, Ploug M, Kjaer A. New peptide receptor radionuclide therapy of invasive cancer cells: in vivo studies using ^{177}Lu-DOTA-AE105 targeting uPAR in human colorectal cancer xenografts. *Nucl Med Biol.* 2012;39:962–969.

26. Persson M, Juhl K, Rasmussen P, et al. uPAR targeted radionuclide therapy with ^{177}Lu-DOTA-AE105 inhibits dissemination of metastatic prostate cancer. *Mol Pharm.* 2014;11:2796–2806.

27. Persson M, Gedda L, Lundqvist H, et al. [^{177}Lu]pertuzumab: experimental therapy of HER-2-expressing xenografts. *Cancer Res.* 2007;67:326–331.

28. Hong H, Zhang Y, Nayak TR, et al. Immuno-PET of tissue factor in pancreatic cancer. *J Nucl Med.* 2012;53:1748–1754.

29. Shi S, Hong H, Orbay H, et al. ImmunoPET of tissue factor expression in triple-negative breast cancer with a radiolabeled antibody Fab fragment. *Eur J Nucl Med Mol Imaging.* 2015;42:1295–1303.

30. Viola-Villegas NT, Sevak KK, Carlin SD, et al. Noninvasive imaging of PSMA in prostate tumors with [89]Zr-labeled huJ591 engineered antibody fragments: the faster alternatives. *Mol Pharm.* 2014;11:3965–3973.

31. Dearling JLJ, Voss SD, Dunning P, et al. Imaging cancer using PET: the effect of the bifunctional chelator on the biodistribution of a ^{64}Cu-labeled antibody. *Nucl Med Biol.* 2011;38:29–38.

32. Petersen LC, Nørby PL, Branner S, et al. Characterization of recombinant murine factor VIIa and recombinant murine tissue factor: a human-murine species compatibility study. *Thromb Res.* 2005;116:75–85.

33. Knudsen T, Olsen OH, Petersen LC. Tissue factor and factor VIIa cross-species compatibility. *Front Biosci (Landmark Ed).* 2011;16:3196–3215.

34. Erhardtsen E, Nilsson P, Johannessen M, Thomsen MS. Pharmacokinetics and safety of FFR-rFVIIa after single doses in healthy subjects. *J Clin Pharmacol.* 2001;41:880–885.

35. Delbeke D, Coleman RE, Guiberteau MJ, et al. Procedure guideline for tumor imaging with ^{18}F-FDG PET/CT 1.0. *J Nucl Med.* 2006;47:885–895.